

Structural Determination of a Filamentous Chaperone to Fabricate Electronically Conductive Metalloprotein Nanowires

Yun X. Chen, Nicole L. Ing, Fengbin Wang, Dawei Xu, Nancy B. Sloan, Nga T. Lam, Daniel L. Winter, Edward H. Egelman, Allon I. Hochbaum, Douglas S. Clark, and Dominic J. Glover*



Cite This: *ACS Nano* 2020, 14, 6559–6569



Read Online

ACCESS |



Metrics & More



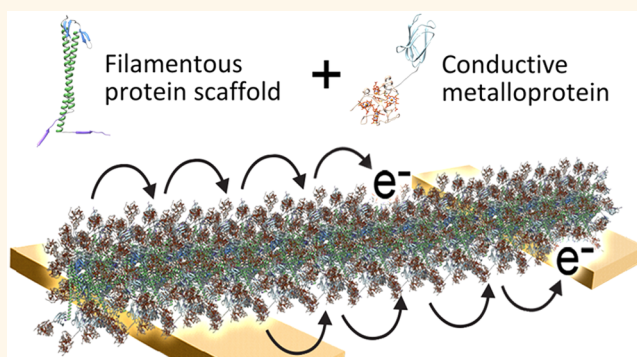
Article Recommendations



Supporting Information

ABSTRACT: The transfer of electrons through protein complexes is central to cellular respiration. Exploiting proteins for charge transfer in a controllable fashion has the potential to revolutionize the integration of biological systems and electronic devices. Here we characterize the structure of an ultrastable protein filament and engineer the filament subunits to create electronically conductive nanowires under aqueous conditions. Cryoelectron microscopy was used to resolve the helical structure of gamma-prefoldin, a filamentous protein from a hyperthermophilic archaeon. Conjugation of tetra-heme c3-type cytochromes along the longitudinal axis of the filament created nanowires capable of long-range electron transfer. Electrochemical transport measurements indicated networks of the nanowires capable of conducting current between electrodes at the redox potential of the cytochromes. Functionalization of these highly engineerable nanowires with other molecules, such as redox enzymes, may be useful for bioelectronic applications.

KEYWORDS: conductive biomaterials, electron transport, nanowires, protein engineering, protein self-assembly



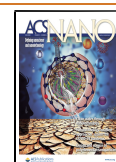
Electron transfer (ET) through protein complexes is a central process of life for the storage and use of energy in many biological systems. For example, photosynthesis requires long-range ET to convert solar energy into chemical energy. Natural bacterial biofilms have been discovered that are able to transfer electrons efficiently to extracellular acceptors, such as iron oxides.¹ These biofilms are made of a network of nanowires that function as conduits for ET-related respiration and metabolism.^{2,3} Bacterial nanowire ET is generally described by theories of electron hopping or tunnelling along the nanowire between redox species such as cytochrome *c* (cyt) proteins or π – π stacked aromatic amino acids.⁴ While models have existed for such stacked amino acids in bacterial type 4 pili, a recent study has shown that the intensively studied *Geobacter sulfurreducens* nanowires are actually a polymer of hexaheme cyt *c* proteins, and not type 4 pilin.⁵ Sequential electron hopping or tunneling processes give rise to long-distance ET, which for bacterial nanowires can be several micrometers. Although naturally occurring bacterial nanowires may be useful conductive materials, these complex assemblages are difficult to engineer and repurpose, and the mechanism of their ET is not well-understood.

Exploiting the ability of proteins to self-assemble into material templates may enable replication of the ET observed in bacterial nanowires in a well-controlled and tunable platform for bioelectronics.^{6,7} Advances in protein design have enabled the creation of supramolecular architectures of controllable size and symmetry,⁸ which can potentially be used to align cyt *c* proteins for long-range ET to other functional materials. A recently described approach for building protein templates used engineered connector proteins to control the assembly of ultrastable filaments into geometrical structures that served as scaffolds for nanomaterials.⁹ The filamentous protein, called gamma-prefoldin (γ PFD), is produced by *Methanocaldococcus jannaschii*, a hyperthermophilic archaeon.^{10,11} Prefoldins are molecular chaperones found in archaea

Received: November 28, 2019

Accepted: April 29, 2020

Published: April 29, 2020



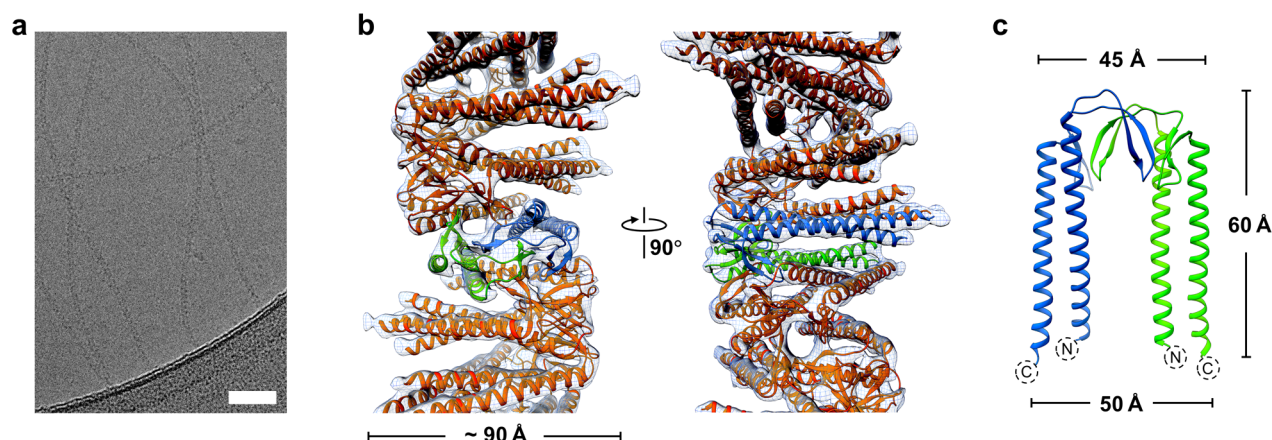


Figure 1. Cryo-EM reconstruction of the *Methanocaldococcus jannaschii* γ PFD filament structure. (a) Cryo-EM micrographs of γ PFD filaments. Scale bars = 50 nm. (b) Three-dimensional helical reconstruction of γ PFD. The γ PFD protein is shown in orange, and two subunits in a dimer assembly are highlighted in blue and green, respectively. The map resolution was filtered to 6.0 Å. (c) The γ PFD dimer is shown with the 2-fold axis relating the two subunits in the plane of the figure.

and eukaryotes that generally have a jellyfish-like hexameric structure. Unusually, γ PFD assembles into filaments of up to 3 μ m in length composed of homomeric protein subunits, with homology modeling suggesting the subunits assemble through β -sheets with the remainder of the protein protruding as a coiled-coil domain.¹² Filaments of γ PFD have several advantages as scaffolds for nanomaterials including high thermal stability ($T_m = 93^\circ\text{C}$),¹³ inherent chaperone activity,¹² and affinity for metals.^{9,13} Furthermore, the interface of the protein is highly malleable, which can be redesigned to impart specificity and drive filament assembly into multifaceted and ordered structures.^{9,14} The resulting branched assemblies of γ PFD have been used to template gold nanoparticles to create conductive metallic architectures.⁹

Herein, we expanded the use of γ PFD to position and align multiheme cytc metalloproteins to mimic the electron-hopping ET observed in *G. sulfurreducens* nanowires. The structure of the γ PFD filament subunits was resolved by cryoelectron microscopy (cryo-EM) to a 6 Å resolution, which provided guidance for the design of proteins to attach and align cytc proteins using SpyTag-SpyCatcher chemistry. Subsequently, we demonstrated that a network of these metalloprotein nanowires conducts current under aqueous conditions through the cytc domains at their redox potential.

RESULTS AND DISCUSSION

Cryo-EM Structural Determination of Filamentous γ PFD. Application of γ PFD as a template to align metalloproteins with precision requires an improved understanding of the filament structure. Cryo-EM was therefore used to determine the three-dimensional structure of recombinantly produced γ PFD filaments (Figure 1a). An averaged power spectrum from approximately 17 000 overlapping cryo-EM image segments of γ PFD (Figure S1) showed a meridional layer line at $\sim 1/(18\text{ Å})$, establishing that the rise per subunit is $\sim 18\text{ Å}$, and a 1-start layer line at $\sim 1/(21\text{ Å})$, which together define a helical symmetry unambiguously, except for an enantiomorphic ambiguity (*i.e.*, whether the 1-start is right- or left-handed). Using the iterative helical real space reconstruction (IHRSR) approach¹⁵ and particle polishing,¹⁶ a resolution was reached where the handedness of the γ PFD coiled-coil was visible. Subsequently, we determined that the

coiled-coil is a left-handed 1-start helix with a rise per subunit of 18.3 Å and a rotation of -48.9° along this helix (Figure 1b). In addition, a γ PFD homodimer was observed in the asymmetric helical subunit, with the 2-fold axis of the homodimer perpendicular to the filament axis; hence, the filament assembly is bipolar (Figure 1c). Applying dihedral symmetry slightly improved the resolution of the cryo-EM reconstruction, enabling us to resolve that the filament termini are identical. An atomic model was built of γ PFD from an initial structure obtained by homology modeling, using the α PFD subunit in PDB 2ZDI as the template.¹⁷ Residues 8–128 were built into the cryo-EM density map, but several residues at both termini could not be included due to loop flexibility. After the model building, we directly estimated the map resolution using a model:map comparison,¹⁸ which yielded an estimate of 6.0 Å (Figure S2). The “gold standard” map:map Fourier shell correlation and the recently described parameter d99¹⁹ also gave a similar resolution estimate (Table S1).

As the paralogous gene of α PFD, the architecture of a single γ PFD subunit is structurally similar to other α PFD structures.¹⁰ The reconstituted γ PFD subunit model has two long α -helices from the N- and C-terminal regions that form a $\sim 60\text{ Å}$ long antiparallel coiled-coil, and those long helices are connected by two β hairpins (Figure 1c). A structural similarity search by DALI²⁰ returns two archaeal α PFD structures with high percentage sequence coverage (Figure 2a). Compared with the α PFD dimers, the angle between the two coiled-coils in γ PFD dimers is about 10° smaller (Figure 2b). The two archaeal α PFDs have been shown to form heterohexamers with β PFD subunits with a “jellyfish”-like quaternary structure (Figure 2c).^{17,21} The α PFD/ β PFD hexamer is held together by two β -barrels, and each β -barrel contains four β -hairpins from two α PFD and two β PFD subunits. Despite γ PFD and the two α PFD proteins having similar secondary structure and $\sim 20\%$ sequence identities with each other, γ PFD does not assemble with either α PFD or β PFD subunit *in vitro*.¹⁰ Instead γ PFD self-polymerizes *in vitro* into long filaments (Figure 1b), suggesting that this is the native assembly of γ PFD.

The buried surface area of a single γ PFD subunit in the β -barrel and loop region was calculated using PISA²² to be about 2100 Å^2 , suggesting the β -barrel is primarily responsible for filament assembly. Strikingly, dimers of γ PFD are rotated 50°

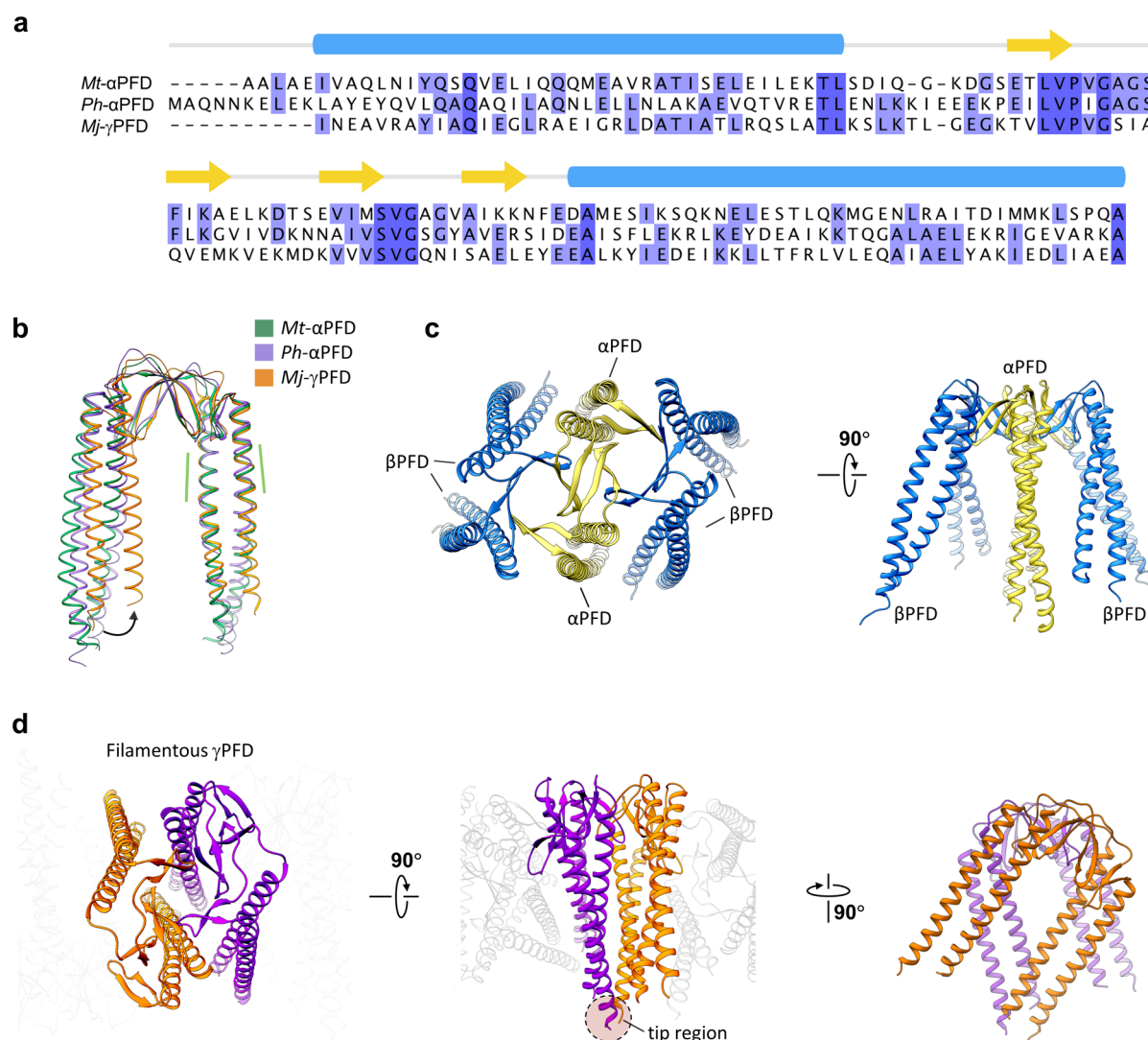


Figure 2. Comparison between filamentous γ PFD and the α PFD- β PFD hexamer solved previously by X-ray crystallography (PDB 1FXK). (a) Structure-based sequence alignment of α PFD from *Methanothermobacter thermautotrophicus* (Mt), α PFD from *Pyrococcus horikoshii* (Ph), and γ PFD from *Methanocaldococcus jannaschii* (Mj). Only the sequences determined in the X-ray/cryo-EM structures are shown, and the corresponding secondary structure is shown above the sequence (α -helical domains in blue and β -sheets in yellow arrows). (b) Structure alignment of the α PFD/ γ PFD dimer described in (a). The region used for structural alignment is highlighted by green dashed lines. (c) “Jellyfish”-like quaternary structure of the α PFD- β PFD hexamer in PDB 1FXK.²¹ The α PFD subunits are colored yellow, and the β PFD subunits are blue. (d) Filamentous structure of the γ PFD highlighting two adjacent dimers with their interactions shown from varying angles.

along the helical axis with neighboring dimers (Figure 2d), which contrasts with the α PFD- β PFD hexamer, where the α PFD dimer is almost parallel to the β PFD dimer. As a result, the coiled-coil region of γ PFD may also contribute to polymerization, and the buried surface area of the coiled-coil region in a single γ PFD subunit is about 620 Å², which contributes to ~23% of its total buried surface. Furthermore, the helical twist brings the tips of two coiled-coils together, and extra density can be seen at the tip region that corresponds to the extra residues not built in the atomic model. It is notable that the helical filament structure determined from cryo-EM differs from the hypothetical nonhelical, brush-like structure proposed in previous studies.^{9,12}

Despite the helical arrangement of coiled-coils, filaments of γ PFD have comparable chaperone activity to archaeal α/β hexameric prefoldins,¹⁰ including filaments engineered to contain only six subunits.¹² The reason for the helical assembly

of γ PFD is unclear; presumably the filament has additional functions within *M. jannaschii*. Other archaeal chaperones, such as chaperonins, have been shown to form filaments *in vivo* and have been proposed to have cytoskeleton function for cell shape determination and division.^{23,24} Filaments of γ PFD whose average length is sufficient to span the diameter of *M. jannaschii* may also have similar cytoskeleton roles.

The significant buried surface area of the γ PFD coiled-coils and the extra density at the tip region observed in cryo-EM strongly suggest the distal regions of the coiled-coils are involved in filament oligomerization. A previous study demonstrated that γ PFD with truncated coiled-coils was still able to assemble into filaments; however, the filaments were significantly longer and stiffer than wild-type filaments.²⁵ It may be that intermolecular interactions of the coiled-coils sterically hinder the alignment and incorporation of incoming subunits to the helical structure of the protofilament; similar

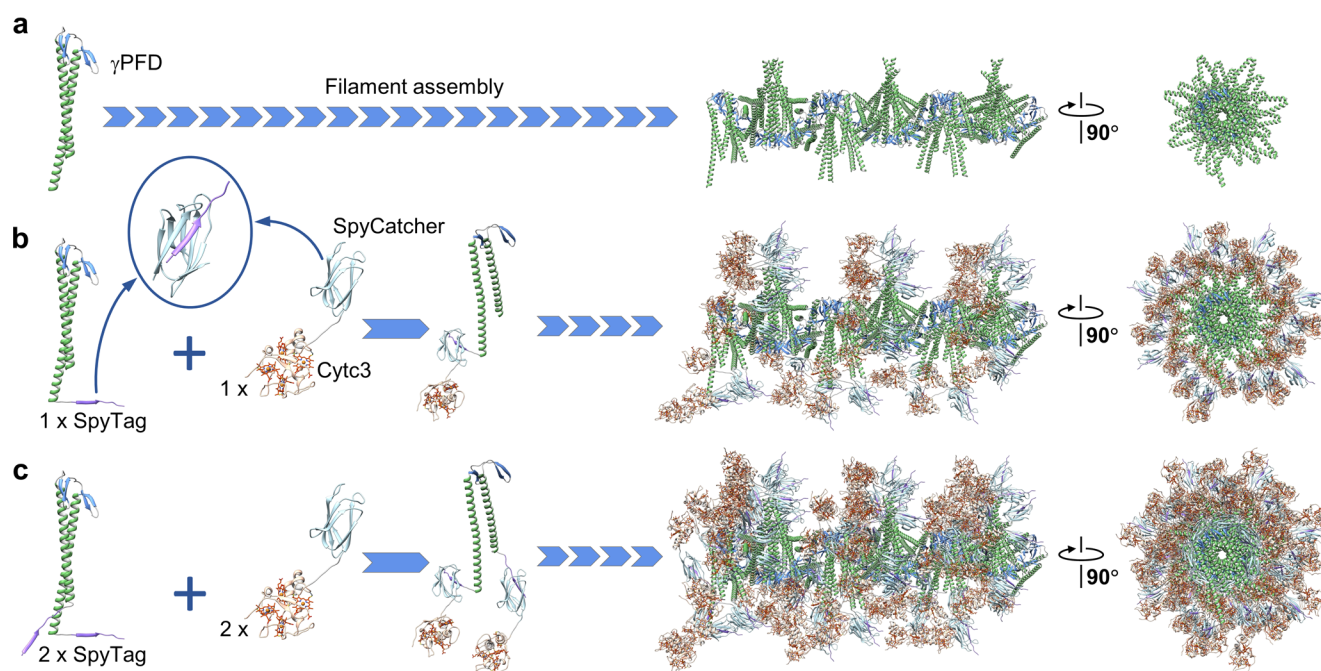


Figure 3. Design and assembly strategy of metalloprotein nanowires. (a) Proposed structure of γ PFD filaments with full-length coiled-coils. Inclusion of a SpyTag domain at (b) the C-terminus or (c) both termini of γ PFD subunits enables covalent attachment of one or two cytc3-SpyCatcher proteins. The fused protein subunits assemble as metalloprotein nanowires.

processes have been observed for the oligomerization of other filamentous proteins.^{26,27} The ability to tailor γ PFD filament length and stiffness by truncation of its coiled-coil domain may be a useful property in a material scaffold.

Design and Fabrication of γ PFD–Metalloprotein Nanowires. Exploiting the close spacing of the γ PFD coiled-coils should enable precise alignment of functional molecules, such as redox proteins, along the lateral direction of the filaments. The cryo-EM-resolved structure of γ PFD filaments enabled us to design metalloprotein filaments to position and align cytc domains for mimicking the electron-hopping mechanism of *G. sulfurreducens* nanowires. A predicted model of the full-length γ PFD monomer was created by adding the residues at both termini that could not be resolved in the cryo-EM map due to loop flexibility (Figure 3a). The tetraheme cytc3 from *Desulfovibrio vulgaris* Miyazaki was chosen to mediate conductance.²⁸ The amide bond forming SpyTag-SpyCatcher chemistry enables efficient and specific conjugation between proteins tagged with the 13-residue SpyTag peptide and counterpart proteins fused to the 12 kDa SpyCatcher domain.^{29,30} In the first designs, the SpyTag sequence was genetically fused to the C-terminal of γ PFD, and the SpyCatcher domain genetically fused to the C-terminal of cytc3 (Figure 3b). Incubation of the cytc3-SpyCatcher with γ PFD-SpyTag filaments should result in spontaneous conjugation between the SpyTag-SpyCatcher domains, completing the self-assembly of the metalloprotein nanowires. The spacing between the coiled-coil of γ PFD dimers along the longitudinal axis is sufficient to accommodate the approximate 40 Å diameter of the cytc3 subunit, which when attached to γ PFD-SpyTag filaments, should result in cytc3 molecules positioned adjacent to each other along the entire filament. Furthermore, in our modeling of the nanowires (Figure 3b), the abundance in electron-transporting hemes should ensure the distance between redox sites of adjacent cytc3 is less than 25 Å, the physical threshold for efficient

electron hopping.³¹ In our model, the minimum edge-to-edge distance between the hemes of adjacent cytc3 domains on the C-terminal of γ PFD can vary from 13.2 to 19.1 Å (Figure S3a). The varying distances of cytc3 domains are likely due to the dynamic flexibility of the γ PFD coiled-coil and short linker regions that join the γ PFD, SpyTag, SpyCatcher, and cytc3 domains. A greater density of cytc3 may increase conductance by staggering or spatially confining cytc3 domains in closer proximity for more efficient ET between heme molecules. To examine the effect of additional cytc3 on the nanowire for ET, a design was created with SpyTag domains at both termini of γ PFD to facilitate the attachment of two cytc3 per γ PFD subunit (Figure 3c). Nanowires containing one cytc3 per γ PFD subunit were designated γ PFD-cytc3, and nanowires containing two cytc3 per subunit were designated γ PFD-[cytc3]₂. In the γ PFD-[cytc3]₂ model, the minimum edge-to-edge distances between hemes of adjacent cytc3 domains on the C-terminal of γ PFD were similar to the γ PFD-cytc3 model, with distances ranging from 13.8 to 21.1 Å (Figure S3b). Furthermore, in the γ PFD-[cytc3]₂ model, the N-terminal cytc3 domains are staggered in proximity (14.9 to 18.7 Å) to the C-terminal cytc3 domains of subunits positioned further along the filament (Figure S3c), thereby potentially providing smaller interheme distances for more efficient ET.

The gene sequences of fusion proteins were chemically synthesized and cloned into plasmid DNAs for recombinant expression in *E. coli*. Purified subunits of γ PFD containing one or two SpyTag domains were assembled into filaments at 60 °C and conjugated with cytc3-SpyCatcher subunits. Non-conjugated cytc3-SpyCatcher protein could be removed by attaching the nanowires to Ni-NTA through the hexa-histidine tag on the γ PFD and washing away unbound proteins. Efficient conjugation of cytc3-SpyCatcher to the SpyTag domain was verified by SDS-PAGE (Figure S4). Conjugation of the 20 kDa γ PFD-SpyTag with the 28 kDa cytc3-SpyCatcher produced a

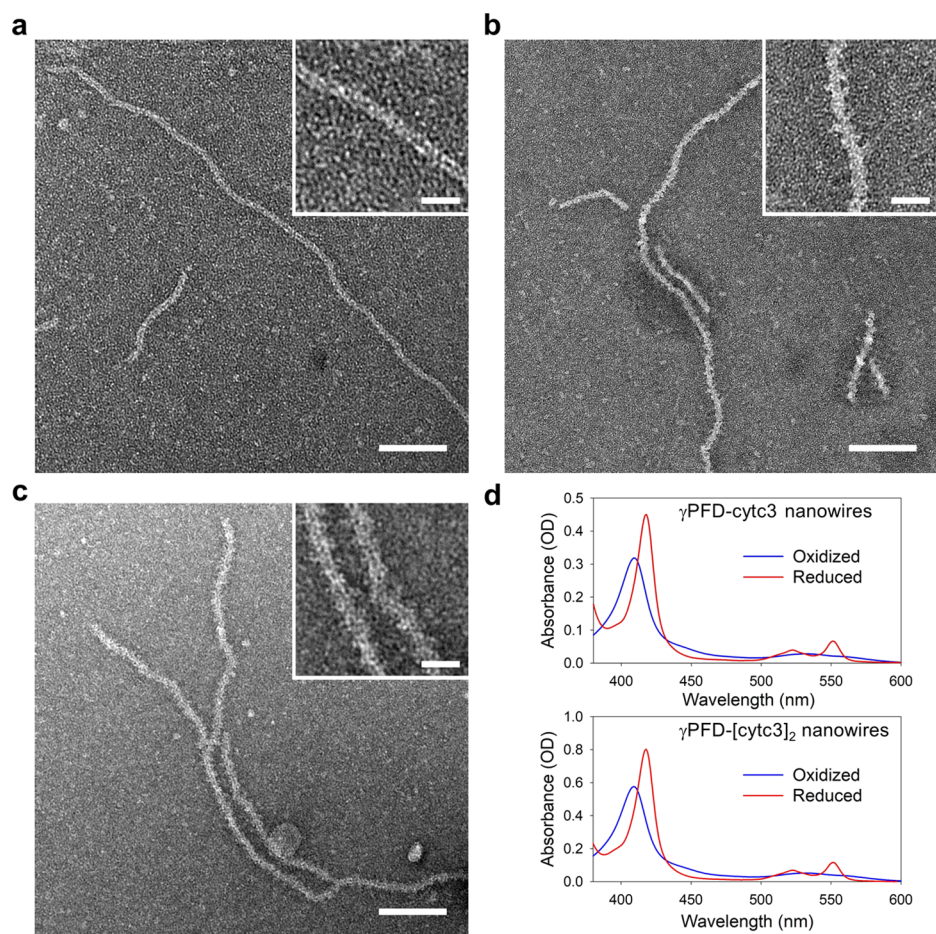


Figure 4. Imaging of metalloprotein nanowires. (a) TEM micrographs of γ PFD filaments and (b) γ PFD-cytc3 and (c) γ PFD-[cytc3]₂ metalloprotein nanowires. Scale bars = 100 nm. Inset micrographs are enlarged images of nanowires showing differences in morphology. Scale bars = 20 nm. (d) Absorption spectra of the γ PFD-cytc3 (top) and γ PFD-[cytc3]₂ (bottom) nanowires in an air-oxidized or reduced state by addition of sodium borohydride.

new band with a cumulative mass of 48 kDa in the SDS-PAGE gel.

The nanowires were imaged by negative-stain TEM and compared with γ PFD-SpyTag filaments (Figure 4a). Distinct structural differences along the lateral edges of the cytc3-conjugated filaments were observed for both the γ PFD-cytc3 (Figure 4b) and γ PFD-[cytc3]₂ nanowires (Figure 4c). The helical structure of the filament should result in bound cytc3-SpyCatcher domains being symmetrically arranged around the filament (Figure 3), which is consistent with the structures imaged in TEM (Figure 4). The metalloprotein nanowires displayed Gaussian distributions of filament lengths in TEM (Figure S5), with an average length of 292 nm for the γ PFD-cytc3 and 274 nm for the γ PFD-[cytc3]₂ ($n = 130$ filaments). Increased thickness of the nanowires from cytc3 conjugation was also observed by atomic force microscopy (AFM), with height measurements averaging 2.8 and 3.6 nm for the γ PFD-cytc3 and γ PFD-[cytc3]₂, respectively, compared with 2.2 nm for the γ PFD-SpyTag filaments (Figure S6). Cryo-EM reconstruction was also attempted for the metalloprotein nanowires; however, the conjugated cytc3-SpyCatcher domains were too structurally flexible on the filament to resolve a structure.

The redox characteristics of cytc3 within the nanowires were measured by UV-vis absorption spectroscopy (Figure 4d). In their air-oxidized state, the absorption spectrum of the cytc3-

containing nanowires displayed a dominant Soret peak at 409 nm, characteristic of ferric heme configurations of cytc3 when Fe(III) ions are chelated to the porphyrin molecule.²⁸ The Soret peak shifted from 409 to 418 nm after addition of a reducing agent, sodium borohydride, which is representative of electron transfer to the iron core of the heme, as changes in bond energy within the porphyrin ligand introduce variations in the absorption spectrum.³² Correspondingly, α and β bands, at 522 and 551 nm, respectively, were observed upon reduction and are characteristic features of low-energy transitions in the porphyrin under reduced state of the heme.³³

Charge Transport Measurements of the Metalloprotein Nanowires. Solid-state and electrochemical ET measurements were performed on films of the metalloprotein nanowires and controls. For both measurements, nanowire samples were cast as dried films onto interdigitated electrodes separated by 6.25 μ m spacing. In these film measurements, conductivity will be affected by several factors, such as the stacking density and orientation of the cytc3 and the density of the percolation network of filaments. Deposited films of γ PFD-cytc3 and γ PFD-[cytc3]₂ nanowires were shown to exhibit long-range electronic conductivity by establishing a percolating network of filaments spanning the electrode gaps,³⁴ with incorporation of the cytc3 shown to be critical for conductivity (Figure S7). Dry films composed of either cytc3-SpyCatcher or γ PFD-cytc3 are 3.7- or 5.5- to 6.4-fold more conductive than

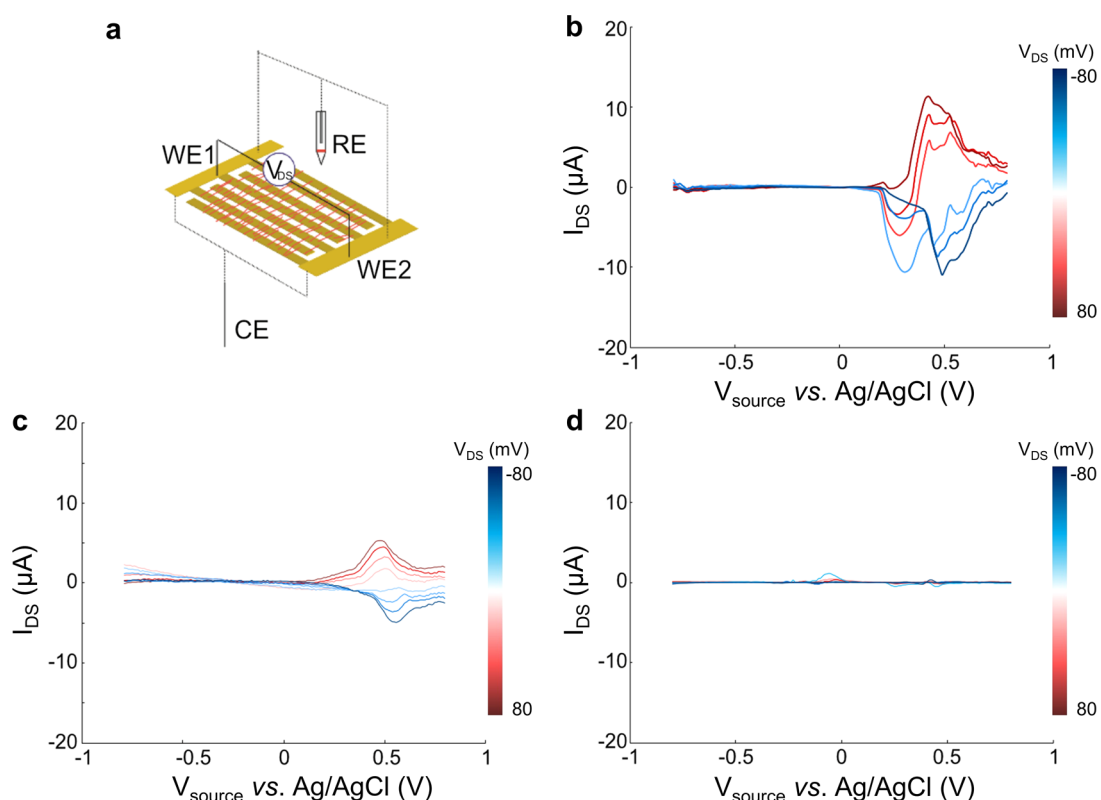


Figure 5. Bipotentiostat cyclic voltammogram measurements of nanowires and controls. (a) Device schematic demonstrating nanowires deposited across electrodes (working electrodes 1 and 2, WE1 and WE2; reference electrode, RE; counter electrode, CE). WE1 and WE2 are the “source” and “drain” electrodes, respectively. (b) γ PFD-cytc3 nanowire, (c) cytc3-SpyCatcher, (d) γ PFD-SpyTag. All measurements were performed at a scan rate of 50 mV/s in 0.1 M phosphate buffer, pH 8.4.

γ PFD-SpyTag alone, respectively. The greater conductivity of films composed of γ PFD-cytc3 nanowires compared with films composed of cytc3-SpyCatcher suggest that the γ PFD scaffold may be aligning the cytc3 in a more efficient arrangement for multistep charge transfer or enhancing the percolation networks of cytc3 domains, compared to those present in a randomly deposited cytc3 film. Although the γ PFD-[cytc3]₂ nanowire has twice the number of cytc3 molecules aligned along the filament compared with the γ PFD-cytc3 (Figure 2c), the γ PFD-[cytc3]₂ was only 12–16% more conductive. Cyclic voltammetry (CV) was used to measure current between a single working electrode and a Pt counter electrode with a Ag/AgCl reference to provide insight into the charge transfer process in γ PFD-cytc3 nanowires. The peak current for γ PFD-cytc3 films was proportional to the square root scan rate, which is indicative of a diffusion-limited redox process (Figure S8). This observation is consistent with a gradient-driven redox transport that has also been observed in *G. sulfurreducens* biofilms, which incorporate extracellular cytc domains.³

Bipotentiostat cyclic voltammograms were used to investigate the magnitude and nature of ET through the γ PFD-cytc3 nanowire films under physiologically relevant conditions. Bipotentiostat measurements have previously been used to distinguish between redox- and nonredox-mediated charge transport in conductive materials.^{7,34,35} Briefly, in this setup (Figure 5a), the global (gate) potential of both the source and drain electrodes is swept relative to a Ag/AgCl reference electrode, while maintaining a fixed potential offset between the source and drain. The source and drain are two working electrodes that share a common counter electrode. The

source–drain current, I_{DS} , is half the difference of the separate source and drain currents at a fixed V_{DS} offset, minus background currents at $V_{DS} = 0$. For ease of viewing, the oxidation peaks during the anodic scan are provided in Figure 5, and the full anodic and cathodic bipotentiostat I_{DS} currents are provided in Supporting Figure S9.

The bipotentiostat measurements show that the γ PFD-cytc3 nanowire and cytc3-SpyCatcher films conduct current between the source and drain electrodes at similar redox potentials. From the individual CVs of each electrode, the redox peaks for cytc3-SpyCatcher occur around $E_{ox} = 0.6$ V, $E_{red} = -0.14$ V vs Ag/AgCl and around $E_{ox} = 0.5$ V and $E_{red} = -0.1$ V for γ PFD-cytc3 (Figure S9). As shown in Figure 5b and c, the bipotentiostat I_{DS} peaks for the γ PFD-cytc3 nanowire and cytc3-SpyCatcher films during the anodic scan are centered around these potentials, with the magnitude and direction of the current tracking with the magnitude and polarity of V_{DS} . Conversely, the I_{DS} current does not scale with V_{DS} magnitude or polarity for the nonconducting γ PFD-SpyTag film (Figure 5, Figure S9). These measurements suggest that the nanowire film is conducting current between the source and drain electrodes through the cytc3 domains. The currents through the γ PFD-cytc3 films are larger than current through a film composed entirely of cytc3-SpyCatcher (Figure 5c), consistent with the solid-state measurements. Furthermore, current exchange happens at similar redox potentials, suggesting that ET in both the γ PFD-cytc3 and cytc3-SpyCatcher samples occurs through the same cytc3 heme states. Small, unexpected redox peaks were also observed in the γ PFD-SpyTag nanofiber films at -0.04 and 0.42 V vs Ag/AgCl, which may account for

the small differences in redox values between the cytc3-SpyCatcher and γ PFD-cytc3 systems. Although the nanowire scaffold does not appear to conduct redox current through the source and drain electrodes, it evidently enhances current exchange between the working electrodes when coupled with cytc3. The mechanism of enhanced conduction is unclear, but it may stem from an increase in conductive bridge formation within the cytc3 network by alignment on the γ PFD scaffolds, as compared to similar densities of unaligned cytc3 in the films of cytc3-SpyCatcher.

Differences in current transport between γ PFD-cytc3 and control films were more apparent in solution than in solid-state measurements. These differences may be attributed to one or several of the following reasons: (1) the aqueous solution provides a more physiologically relevant environment to support redox hopping through native conformation cytc3, (2) the use of a reference in the electrochemical setup guarantees that the measurement sweeps through the redox potential of the cytc3 domains, and (3) all films experienced partial delamination, since there was a visible reduction of material after measurements in solution, but differences in delamination were not characterized. Films composed of γ PFD-SpyTag lacking cytc3 domains exhibited negligible charge transfer between the source and drain electrodes (Figure 5d), indicating that cytc3 is the primary conductive component in the γ PFD-cytc3 nanowire films.

CONCLUSIONS

The present study solved the structure of γ PFD to 6 Å resolution and engineered these filaments to create modular metalloprotein nanowire films capable of facilitating long-range ET. Mimicking the ET of *G. sulfurreducens* nanowires requires a structural scaffold to align cytc metalloproteins in proximity over long distances. The ultrastable and engineerable γ PFD filament was chosen as a scaffold, and its structure resolved by cryo-EM, which also provided insights into filamentous arrangements of prefoldins. As a class of molecular chaperones, prefoldins function in an ATP-independent manner to arrest protein misfolding in archaea and participate in the maturation of cytoskeletal proteins in eukaryotes.¹¹ Except for γ PFD, prefoldins assemble into heterohexameric complexes composed of two α -type and four β -type subunits.²¹ The overall hexameric quaternary structure consists of a rigid double β -barrel with six highly flexible coiled-coils extending outward in the same direction. Previous homology modeling of γ PFD using archaeal α PFD as a template supported a nonhelical, brush-like structure for the filaments.^{9,12} The helical filament structure of γ PFD determined from cryo-EM in this study was thus unexpected and is unique among molecular chaperones and filamentous proteins in general.

The resolved structure of γ PFD enabled the design of nanowires for the alignment of cytc3 proteins in high density. The modular SpyTag-SpyCatcher chemistry used to attach cytc3 to γ PFD should enable a variety of other metalloproteins to be aligned on the filaments. Other redox proteins including iron–sulfur, zinc, or copper metalloproteins could be incorporated into γ PFD filaments in place of the cytc3 to tune the electrical and semiconductor properties of the nanowires. The ability to customize the redox properties of metalloprotein nanowires would be useful for specific bioelectronic applications or for interrogating the underlying mechanisms of charge transport in biomaterials. The distance between the hemes of the cytc3 domains was sufficient for ET,

which was most likely mediated by an electron-hopping mechanism. However, the flexibility of the SpyTag-SpyCatcher domains permits mobility of the cytc3 domains, which suggests that diffusion-assisted hopping mechanisms may also be occurring for conductance.⁴

In addition to assembly into linear nanowires, the individual γ PFD-cytc3 subunits are building blocks that could potentially be used to construct conductive nanostructures or interface with other functional materials. Previously, it has been demonstrated that multiple γ PFD filaments can be joined using engineered connector proteins.⁹ These connectors would enable the nanowires to be assembled into ordered structures or enable attachment of functional molecules, such as redox enzymes, at specific locations, for applications in fuel cells or biosensors. Furthermore, the interface of γ PFD can be redesigned to create subunits that assemble in repeating orders to create multicomponent filaments.¹⁴ These filaments would enable a variety of metalloproteins with different redox potentials to be aligned in specific orders, potentially mimicking natural electron transport chains. The modularity and engineerability of γ PFD metalloprotein nanowires hold potential for application as naturally inspired bioelectronic materials.

METHODS

Cryo-EM Data Collection and Image Processing. The wild-type γ PFD was expressed in *E. coli* and purified as described previously.⁹ The γ PFD filament sample (4 μ L at 0.2 mg mL⁻¹) was applied to discharged lacey carbon grids and plunge frozen using a VitroBot Mark IV (FEI). Frozen grids were imaged in a Titan Krios at 300 keV and recorded with a Falcon III camera at 1.09 Å per pixel. Micrographs were collected using a defocus range of 1.5–2.5 μ m, with a total exposure time of 2.4 s (amounting to \sim 55 electrons/Å²) distributed into 24 fractions. All the micrographs were first motion corrected (ignoring the first fraction) using MotionCorr v2.1³⁶ and then used for CTF estimation by the CTFFIND3 program.³⁷ Filament images were extracted using the e2helixboxer program within EMAN2³⁸ from the dose-weighted fractions 2–10 (amounting to \sim 20 electrons/Å²), after the images were corrected for the CTF through multiplication by the theoretical CTF. A total of 32 227 overlapping 384 px long segments (with a shift of 25 pixels, \sim 1.5 times the axial rise per subunit) were generated. The helical symmetry was determined unambiguously given the 1/(18 Å) meridional layer line. The IHRSR method implemented in Spider¹⁵ was used to generate a \sim 7 Å reconstruction, with the volume subsequently filtered to 10 Å as the starting reference used in Relion.¹⁶ The same micrographs and box coordinates used in the Spider reconstruction were imported into Relion. A comparable \sim 7 Å reconstruction was generated after class2D and refine3D steps, and then it was further improved to 6 Å after movie refinement and particle polishing steps. Model:map FSC¹⁸ and d99¹⁹ were used to determine a resolution of the final volume, which was sharpened with a negative B-factor of 200.

Model Building of γ PFD Filaments. The density corresponding to a γ PFD dimer was segmented from the experimental filament density using UCSF Chimera.³⁹ The initial model of γ PFD was generated by homology modeling using the I-TASSER⁴⁰ server using the α PFD subunit in PDB 2ZDI as the template. Then the coiled-coil part of the initial model was further optimized using CCBUILDER 2.0⁴¹ to maximize the real-space fitting with the cryo-EM density at the coiled-coil region. After this, the γ PFD dimer was docked into the segmented map using Chimera. A filamentous model was generated using this γ PFD dimer as the asymmetric unit and refined against the full cryo-EM map, using real-space refinement in PHENIX.¹⁹ To prevent model overfitting at this resolution, protein secondary structure was restrained during the entire refinement and the coiled-coil region was refined as a rigid body. MolProbity⁴² was used to evaluate the quality of the filament model.

Protein Nanowire Design. UCSF Chimera software (version 1.12)³⁹ was used to build a predicted model of the full-length γ PFD monomer by adding the amino acid sequences VNEVID (residues 2–7) and QQTSEEEKAEEEEENEEKAE (residues 129–147) to the N-terminus and C-terminus that were absent from the cryo-EM-resolved 6 Å resolution model of the wild-type γ PFD structure. The initial methionine residue was omitted due to its cotranslational cleavage in *E. coli*. ϕ (phi) and ψ (psi) torsion angles were adjusted to -57° and -47° , respectively, to ensure an α -helical conformation of the N- and C-termini (Figure 3a).

To create hypothetical models of the γ PFD monomer covalently bound to one or two cytochromes, the model of the full-length γ PFD monomer as well as the available X-ray crystallography structures of the SpyCatcher-SpyTag complex (PDB ID: 4MLI)⁴³ and of cytochrome c3 (cytc3) from *Desulfovibrio vulgaris* Miyazaki F (PDB ID: 2EWK)⁴⁴ were joined using the UCSF Chimera software (Figure 3b). The C-terminus of cytc3 was joined to the N-terminus of the SpyCatcher domain via a GGGs linker to create a model of cytc3 fused to the SpyCatcher-SpyTag complex. Working with this new model, the N-terminus of the SpyTag from the cytc3-SpyCatcher-SpyTag model was fused to the C-terminus of the full-length γ PFD model via a GGGs linker to create the model of the γ PFD monomer fused to a cytc3. Then, an additional cytc3 was added to this model, this time by fusing the C-terminus of the SpyTag domain from the cytc3-SpyCatcher-SpyTag model to the N-terminus of the γ PFD subunit via a GGGs linker (Figure 3c). The models of full-length γ PFD, γ PFD fused to one cytc3, and γ PFD fused to two cytc3 through SpyTag-SpyCatcher attachments were aligned to the resolved cryo-EM structure of the γ PFD filament to create a predicted model of the filament and nanowires. In the nanowire models, torsion angles within the GGGs linkers were adjusted, where required, to eliminate clashes between cytc3 domains and Spy domains. In addition, the cytc3-SpyCatcher construct also included an N-terminal OmpA periplasmic targeting sequence. Hexa-histidine tags were included at the N-terminal of the γ PFD-SpyTag and SpyTag- γ PFD-SpyTag to enable IMAC techniques for protein purification. The amino acid sequences for γ PFD and the designed proteins are provided in Table S2.

Recombinant Production of Designed Proteins. The gene sequences for γ PFD-SpyTag, SpyTag- γ PFD-SpyTag, and cytc3-SpyCatcher were chemically synthesized as gBlock Gene Fragments (Integrated DNA Technologies) and cloned into the bacterial expression vector pET19b (Novagen) via the Gibson Assembly method.⁴⁵ Subsequently, the plasmids were transformed into competent BL21 T7 Express *E. coli* (NEB), with the plasmid encoding cytc3-SpyCatcher cotransformed with pEC86, a chloramphenicol-resistant plasmid containing the heme maturation genes ccmABCDEFGH.⁴⁶

Cultures of BL21 containing either the γ PFD-SpyTag or SpyTag- γ PFD-SpyTag plasmid were grown at 37°C in Luria Broth supplemented with $100\ \mu\text{g mL}^{-1}$ ampicillin. Upon reaching an optical density of 0.6 at A600, protein expression was induced for 16 h at 25°C with the addition of 0.4 mM isopropylthiogalactoside (IPTG). Harvested cells were lysed and clarified by centrifugation for 40 min at 22000g. The γ PFD-SpyTag and SpyTag- γ PFD-SpyTag proteins were purified by immobilized metal affinity chromatography on Ni-NTA resin (ThermoFisher). Eluted fractions were analyzed using SDS-PAGE gels stained by QC Colloidal Coomassie G-250 stain (Bio-Rad). Fractions containing the desired pure protein were pooled, concentrated, and buffer exchanged to PBS buffer (10 mM Na_2HPO_4 , 1.8 mM KH_2PO_4 , 137 mM NaCl, 2.7 mM KCl, pH 7.4) using 10 kDa Amicon Ultra-15 centrifugal filters (Merck), followed by lyophilization and storage at -80°C .

Cultures containing the cytc3-SpyCatcher/pEC86 plasmids were grown at 37°C in 2xYT media containing $100\ \mu\text{g mL}^{-1}$ ampicillin and $34\ \mu\text{g mL}^{-1}$ of chloramphenicol. Upon reaching an optical density of 0.6 at A600, protein expression was induced for 16 h at 25°C with the addition of 30 μM IPTG. A periplasmic protein purification was performed on the harvested cells by resuspension in a solution containing ice-cold 30 mM Tris-HCl, 20% w/v sucrose, 1 mM EDTA,

pH 8.0, and incubated on ice for 30 min, followed by centrifugation at 10000g for 20 min. The supernatant was decanted off, and pelleted cells were suspended in ice-cold 0.5 mM MgCl_2 . The cells were incubated for 30 min on ice and centrifuged to obtain a supernatant containing the periplasmic contents. The periplasmic fraction was purified by cation exchange chromatography using a HiTrap SP Sepharose FF column (GE Healthcare). Eluted fractions were analyzed using SDS-PAGE gels stained by QC Colloidal Coomassie G-250 stain. Fractions containing the pure cytc3-SpyCatcher protein were pooled, concentrated, and buffer exchanged to PBS buffer using 10 kDa molecular weight cutoff Amicon Ultra-15 centrifugal filter units and stored at 4°C .

Assembly of Metalloprotein Nanowires. Lyophilized γ PFD, γ PFD-SpyTag, and SpyTag- γ PFD-SpyTag proteins were resuspended in 8 M guanidinium-HCl, 10 mM NaH_2PO_4 , pH 8.0, and the protein concentrations determined by a modified Bradford assay.⁴⁷ The proteins were refolded by a rapid dilution with PBS buffer to achieve a final protein concentration of $0.5\ \text{mg mL}^{-1}$, and filaments assembled during a 16 h incubation at 60°C . Covalent attachment of cytc3 to the filaments was achieved by combining an equimolar ratio of cytc3-SpyCatcher with γ PFD-SpyTag and a double molar ratio of cytc3-SpyCatcher with the SpyTag- γ PFD-SpyTag. Subsequently, the resulting nanowires were stored at 4°C .

Spectrophotometric Analysis of Nanowires. Nanowire samples were diluted to a final concentration of $0.5\ \text{mg mL}^{-1}$ in 20 mM NaH_2PO_4 , 100 mM NaCl, pH 7.5, and transferred into 3 mL quartz cuvettes. Spectral absorption measurements were performed using a Lambda UV-vis spectrometer (PerkinElmer) between wavelengths 300 to 600 nm. Sample was removed from the spectrophotometer, and 0.5 mg of sodium borohydride added for the reduction of cytc3. After reduction, indicated by the color change of the sample to bright pink, spectrophotometric absorption analysis was repeated on the samples.

Negative-Stain Electron Microscopy of Nanowires. Filament and nanowire samples for TEM were diluted to $40\ \mu\text{g mL}^{-1}$ in PBS before deposition on carbon type-B, 200-mesh copper grids (Ted Pella Inc.), pretreated with an easiGlow glow discharge unit (PELCO). After a 5 min incubation at room temperature, the grids were washed with distilled water and stained with 2% aqueous uranyl acetate (BDH Chemicals) for 7 min. The stain was wicked off with filter paper (Whatman), and grids were left to dry before visualization under a Tecnai G2 20 TEM (FEI). The digitized TEM images were analyzed using ImageJ⁴⁸ (U.S. National Institutes of Health) to measure filament and nanowire length.

Atomic Force Microscopy of Nanowires. Sample specimen holders were prepared by mounting PELCO mica discs (Ted Pella Inc.) on AFM specimen discs (Ted Pella Inc.) using Conductive Silver Liquid (ProSciTech). After drying and overnight curing of the silver glue, the mica substrate was peeled three to four times and 10–20 μL of nanowire sample was applied. After 15 min of air-drying, the substrate was rinsed with Milli-Q water using a fine tip pipet and dried overnight. The specimen was loaded on the magnetic platform in the Dimension SPM ICON (Bruker) equipped with a SCANASYST-AIR probe (Bruker). The probe was lowered until within 1 mm above the sample surface before scanning was operated under peakforce tapping mode. Parameters were adjusted such that force was within 10–15 mV, the scan rate was 0.9 Hz, while the resolution was 512 pixels per line for image dimensions of either 1 or 5 μm squares. Image data were processed and analyzed using the NanoScope Software (Bruker).

Device Preparation for Electronic Property Characterization. Solid-state and electrochemical bipotentiostat measurements were performed using interdigitated electrodes. Each electrode comprised 80 parallel $8\ \mu\text{m} \times 2\ \text{mm}$ long bands with an intraband spacing of 6.25 μm . Devices were photolithographically patterned onto Pyrex wafers with 60 nm Au and a 5 nm Ti adhesion layer deposited by electron beam evaporation (UCSD Nano3 Fabrication Foundry Services). Prior to use, devices were sonicated in washes of acetone, isopropanol, and ultrapure water. Devices were individually tested for shorts prior to sample deposition. For electrochemical measurements, 22-gauge solid core insulated wire leads were

connected to the interdigitated source and drain electrodes using conductive silver epoxy (MG Materials). Exposed electrode and lead connections were sealed with waterproof silicone sealant (DAP all-purpose adhesive sealant). For solid-state and electrochemical charge measurements, 15 μL of sample was deposited onto each device in 5 μL intervals and allowed to dry at 4 $^{\circ}\text{C}$. Samples were briefly rinsed with ultrapure water to remove salts prior to measurements.

Solid-State I – V Measurements of Nanowires. Solid state I – V measurements were performed with a Keithley model 2612B source measure unit. Current was monitored as a function of swept voltage from +1 V to –1 V under ambient conditions. Each sample was deposited onto $n = 3$ independent devices. Error bars are reported as the standard error.

Electrochemical Bipotentiostat Measurements of Nanowires. Bipotentiostat measurements were performed in 0.1 M phosphate buffer, pH 8.4, degassed by sparging with 20% CO_2 – N_2 while boiling for an hour. Electrochemical measurements were performed in sealed cells with N_2 flow in the headspace. For each bipotentiostat measurement, the global (gate) potential of the source and drain electrodes was swept relative to a 3.5 M KCl Ag/AgCl reference electrode, while maintaining a fixed potential offset (V_{DS}) between the source and drain, which shared a common Pt counter electrode. The source–drain current, I_{DS} , was taken to be half the difference of the separate source-counter and drain-counter currents at a fixed V_{DS} offset, minus background currents at $V_{\text{DS}} = 0$. Only the anodic (oxidizing) portion of each CV (–0.8 V to +0.8 V vs Ag/AgCl) is shown in Figure 5 for clarity. The full bipotentiostat CVs (anodic and cathodic) are shown in Figure S9. Scans were performed at a scan rate of 50 mV/s.

Electron Microscopy Data. Cryo-EM structural data for the filament were deposited in the Electron Microscopy Data Bank (EMDB) and the Protein Data Bank (PDB) with the following entry codes, EMDB: EMD-21455 and PDB: 6VY1.

ASSOCIATED CONTENT

Supporting Information

The Supporting Information is available free of charge at <https://pubs.acs.org/doi/10.1021/acsnano.9b09405>.

Power spectrum, Fourier shell correlation between the atomic model and the cryo-EM map, proposed spatial alignment of hemes in γPFD –metalloprotein nanowires, SDS-PAGE of cytc3-SpyCatcher conjugation to γPFD -SpyTag, distribution of nanowire lengths, AFM of nanowires, solid-state conductance measurements of nanowires, cyclic voltammogram of γPFD –cytc3 films, individual cyclic voltammograms and bipotentiostat scans, table of refinement statistics for the cryo-EM model, and table of amino acid sequence of γPFD and designed proteins (PDF)

AUTHOR INFORMATION

Corresponding Author

Dominic J. Glover – School of Biotechnology and Biomolecular Sciences, University of New South Wales, Sydney, NSW 2052, Australia; orcid.org/0000-0002-6819-4089; Email: d.glover@unsw.edu.au

Authors

Yun X. Chen – School of Biotechnology and Biomolecular Sciences, University of New South Wales, Sydney, NSW 2052, Australia

Nicole L. Ing – Department of Materials Science and Engineering, University of California, Irvine, California 92697, United States

Fengbin Wang – Department of Biochemistry and Molecular Genetics, University of Virginia, Charlottesville, Virginia 22908, United States

Dawei Xu – Department of Chemical and Biomolecular Engineering, University of California, Berkeley, California 94720, United States

Nancy B. Sloan – Department of Chemical and Biomolecular Engineering, University of California, Berkeley, California 94720, United States

Nga T. Lam – School of Biotechnology and Biomolecular Sciences, University of New South Wales, Sydney, NSW 2052, Australia

Daniel L. Winter – School of Biotechnology and Biomolecular Sciences, University of New South Wales, Sydney, NSW 2052, Australia

Edward H. Egelman – Department of Biochemistry and Molecular Genetics, University of Virginia, Charlottesville, Virginia 22908, United States

Allon I. Hochbaum – Department of Materials Science and Engineering, Department of Chemistry, and Department of Chemical and Biomolecular Engineering, University of California, Irvine, California 92697, United States;

orcid.org/0000-0002-5377-8065

Douglas S. Clark – Department of Chemical and Biomolecular Engineering, University of California, Berkeley, California 94720, United States; Molecular Biophysics and Integrated Bioimaging Division, Lawrence Berkeley National Laboratory, Berkeley, California 94720, United States; orcid.org/0000-0003-1516-035X

Complete contact information is available at:
<https://pubs.acs.org/doi/10.1021/acsnano.9b09405>

Author Contributions

Y.X.C., N.B.S., N.T.L., and D.X. designed and produced the recombinant proteins. F.W. and E.H.E. performed cryo-EM and resolved the filament structure. Y.X.C. characterized the assembly and structure of the nanowires. N.L.I. and A.I.H. performed electrochemical transport measurements. D.L.W. created protein models of the nanowires. D.S.C. and D.J.G. designed and supervised the experimental procedures and wrote the manuscript.

Notes

The authors declare no competing financial interest.

ACKNOWLEDGMENTS

This work was supported by the Air Force Office of Scientific Research (FA9550-17-1-0451 to D.S.C. and D.J.G., FA9550-14-1-0350 to A.I.H.) and the National Institutes of Health GM122510 (to E.H.E.). N.L.I. also acknowledges support from a U.S. Department of Education GAANN fellowship.

REFERENCES

- (1) Reguera, G.; McCarthy, K. D.; Mehta, T.; Nicoll, J. S.; Tuominen, M. T.; Lovley, D. R. Extracellular Electron Transfer via Microbial Nanowires. *Nature* **2005**, *435*, 1098–1101.
- (2) Malvankar, N. S.; Vargas, M.; Nevin, K. P.; Franks, A. E.; Leang, C.; Kim, B.-C.; Inoue, K.; Mester, T.; Covalla, S. F.; Johnson, J. P.; Rotello, V. M.; Tuominen, M. T.; Lovley, D. R. Tunable Metallic-Like Conductivity in Microbial Nanowire Networks. *Nat. Nanotechnol.* **2011**, *6*, 573–579.
- (3) Snider, R. M.; Strycharz-Glaven, S. M.; Tsoi, S. D.; Erickson, J. S.; Tender, L. M. Long-Range Electron Transport in *Geobacter*

Sulfurreducens Biofilms Is Redox Gradient-Driven. *Proc. Natl. Acad. Sci. U. S. A.* **2012**, *109*, 15467–15472.

(4) Ing, N. L.; El-Naggar, M. Y.; Hochbaum, A. I. Going the Distance: Long-Range Conductivity in Protein and Peptide Bioelectronic Materials. *J. Phys. Chem. B* **2018**, *122*, 10403–10423.

(5) Wang, F.; Gu, Y.; O'Brien, J. P.; Yi, S. M.; Yalcin, S. E.; Srikanth, V.; Shen, C.; Vu, D.; Ing, N. L.; Hochbaum, A. I.; Egelman, E. H.; Malvankar, N. S. Structure of Microbial Nanowires Reveals Stacked Hemes That Transport Electrons Over Micrometers. *Cell* **2019**, *177*, 361.

(6) Altamura, L.; Horvath, C.; Rengaraj, S.; Rongier, A.; Elouarzaki, K.; Gondran, C.; Maçon, A. L. B.; Vendrely, C.; Bouchiat, V.; Fontecave, M.; Mariolle, D.; Rannou, P.; Le Goff, A.; Duraffourg, N.; Holzinger, M.; Forge, V. A Synthetic Redox Biofilm Made from Metalloprotein-Prion Domain Chimera Nanowires. *Nat. Chem.* **2017**, *9*, 157–163.

(7) Ing, N. L.; Spencer, R. K.; Luong, S. H.; Nguyen, H. D.; Hochbaum, A. I. Electronic Conductivity in Biomimetic α -Helical Peptide Nanofibers and Gels. *ACS Nano* **2018**, *12*, 2652–2661.

(8) Glover, D. J.; Clark, D. S. Protein Calligraphy: A New Concept Begins to Take Shape. *ACS Cent. Sci.* **2016**, *2*, 438–444.

(9) Glover, D. J.; Giger, L.; Kim, S. S.; Naik, R. R.; Clark, D. S. Geometrical Assembly of Ultraprecise Protein Templates for Nanomaterials. *Nat. Commun.* **2016**, *7*, 11771.

(10) Whitehead, T. A.; Boonyaratanakornkit, B. B.; Höllrigel, V.; Clark, D. S. A Filamentous Molecular Chaperone of the Prefoldin Family from the Deep-Sea Hyperthermophile *Methanocaldococcus Jannaschii*. *Protein Sci.* **2007**, *16*, 626–634.

(11) Lim, S.; Glover, D. J.; Clark, D. S. Prefoldins in Archaea. *Adv. Exp. Med. Biol.* **2018**, *1106*, 11–23.

(12) Glover, D. J.; Clark, D. S. Oligomeric Assembly Is Required for Chaperone Activity of the Filamentous γ -Prefoldin. *FEBS J.* **2015**, *282*, 2985–2997.

(13) Glover, J.; Giger, L.; Kim, R.; Clark, S. Engineering Protein Filaments with Enhanced Thermostability for Nanomaterials. *Biotechnol. J.* **2013**, *8*, 228–236.

(14) Glover, D. J.; Lim, S.; Xu, D.; Sloan, N. B.; Zhang, Y.; Clark, D. S. Assembly of Multicomponent Protein Filaments Using Engineered Subunit Interfaces. *ACS Synth. Biol.* **2018**, *7*, 2447–2456.

(15) Egelman, E. H. A Robust Algorithm for the Reconstruction of Helical Filaments Using Single-Particle Methods. *Ultramicroscopy* **2000**, *85*, 225–234.

(16) Scheres, S. H. W. RELION: Implementation of a Bayesian Approach to Cryo-EM Structure Determination. *J. Struct. Biol.* **2012**, *180*, 519–530.

(17) Ohtaki, A.; Kida, H.; Miyata, Y.; Ide, N.; Yonezawa, A.; Arakawa, T.; Iizuka, R.; Noguchi, K.; Kita, A.; Odaka, M.; Miki, K.; Yohda, M. Structure and Molecular Dynamics Simulation of Archaeal Prefoldin: The Molecular Mechanism for Binding and Recognition of Nonnative Substrate Proteins. *J. Mol. Biol.* **2008**, *376*, 1130–1141.

(18) Subramaniam, S.; Earl, L. A.; Falconieri, V.; Milne, J. L.; Egelman, E. H. Resolution Advances in Cryo-EM Enable Application to Drug Discovery. *Curr. Opin. Struct. Biol.* **2016**, *41*, 194–202.

(19) Afonine, P. V.; Klaholz, B. P.; Moriarty, N. W.; Poon, B. K.; Sobolev, O. V.; Terwilliger, T. C.; Adams, P. D.; Urzhumtsev, A. New Tools for the Analysis and Validation of Cryo-EM Maps and Atomic Models. *Acta Crystallogr., Sect. D: Struct. Biol.* **2018**, *74*, 814–840.

(20) Holm, L.; Laakso, L. M. Dali Server Update. *Nucleic Acids Res.* **2016**, *44*, W351–W355.

(21) Siegert, R.; Leroux, M. R.; Scheufler, C.; Hartl, F. U.; Moarefi, I. Structure of the Molecular Chaperone Prefoldin: Unique Interaction of Multiple Coiled Coil Tentacles with Unfolded Proteins. *Cell* **2000**, *103*, 621–632.

(22) Krissinel, E.; Henrick, K. Inference of Macromolecular Assemblies from Crystalline State. *J. Mol. Biol.* **2007**, *372*, 774–797.

(23) Trent, J. D.; Kagawa, H. K.; Yaoi, T.; Olle, E.; Zaluzec, N. J. Chaperonin Filaments: The Archaeal Cytoskeleton? *Proc. Natl. Acad. Sci. U. S. A.* **1997**, *94*, 5383–5388.

(24) Wagstaff, J.; Löwe, J. Prokaryotic Cytoskeletons: Protein Filaments Organizing Small Cells. *Nat. Rev. Microbiol.* **2018**, *16*, 187–201.

(25) Whitehead, T. A.; Je, E.; Clark, D. S. Rational Shape Engineering of the Filamentous Protein Gamma Prefoldin through Incremental Gene Truncation. *Biopolymers* **2009**, *91*, 496–503.

(26) Fitzpatrick, A. W. P.; Falcon, B.; He, S.; Murzin, A. G.; Murshudov, G.; Garringer, H. J.; Crowther, R. A.; Ghetti, B.; Goedert, M.; Scheres, S. H. W. Cryo-EM Structures of Tau Filaments from Alzheimer's Disease Brain. *Nature* **2017**, *547*, 185–190.

(27) Tanaka, K.; Takeda, S.; Mitsuka, K.; Oda, T.; Kimura-Sakiyama, C.; Maeda, Y.; Narita, A. Structural Basis for Cofilin Binding and Actin Filament Disassembly. *Nat. Commun.* **2018**, *9*, 1–12.

(28) Ozawa, K.; Tsapin, A. I.; Neelson, K. H.; Cusanovich, M. A.; Akutsu, H. Expression of a Tetraheme Protein, *Desulfovibrio Vulgaris* Miyazaki F Cytochrome c3, in *Shewanella Oneidensis* MR-1. *Appl. Environ. Microbiol.* **2000**, *66*, 4168–4171.

(29) Zakeri, B.; Fierer, J. O.; Celik, E.; Chittock, E. C.; Schwarz-Linek, U.; Moy, V. T.; Howarth, M. Peptide Tag Forming a Rapid Covalent Bond to a Protein, through Engineering a Bacterial Adhesin. *Proc. Natl. Acad. Sci. U. S. A.* **2012**, *109*, E690–697.

(30) Lim, S.; Jung, G. A.; Muckom, R. J.; Glover, D. J.; Clark, D. S. Engineering Bioorthogonal Protein-Polymer Hybrid Hydrogel as a Functional Protein Immobilization Platform. *Chem. Commun. (Cambridge, U. K.)* **2019**, *55*, 806–809.

(31) Winkler, J. R.; Gray, H. B. Long-Range Electron Tunneling. *J. Am. Chem. Soc.* **2014**, *136*, 2930–2939.

(32) Wilting, J.; Van Buuren, K. J. H.; Braams, R.; Van Gelder, B. F. The Mechanism of Reduction of Cytochrome c as Studied by Pulse Radiolysis. *Biochim. Biophys. Acta, Bioenerg.* **1975**, *376*, 285–297.

(33) Gouterman, M. Spectra of Porphyrins. *J. Mol. Spectrosc.* **1961**, *6*, 138–163.

(34) Ing, N. L.; Nusca, T. D.; Hochbaum, A. I. *Geobacter Sulfurreducens* Pili Support Ohmic Electronic Conduction in Aqueous Solution. *Phys. Chem. Chem. Phys.* **2017**, *19*, 21791–21799.

(35) Yates, M. D.; Golden, J. P.; Roy, J.; Strycharz-Glaven, S. M.; Tsoi, S.; Erickson, J. S.; El-Naggar, M. Y.; Barton, S. C.; Tender, L. M. Thermally Activated Long Range Electron Transport in Living Biofilms. *Phys. Chem. Chem. Phys.* **2015**, *17*, 32564–32570.

(36) Li, X.; Mooney, P.; Zheng, S.; Booth, C. R.; Braunfeld, M. B.; Gubbens, S.; Agard, D. A.; Cheng, Y. Electron Counting and Beam-Induced Motion Correction Enable Near-Atomic-Resolution Single-Particle Cryo-EM. *Nat. Methods* **2013**, *10*, 584–590.

(37) Mindell, J. A.; Grigorieff, N. Accurate Determination of Local Defocus and Specimen Tilt in Electron Microscopy. *J. Struct. Biol.* **2003**, *142*, 334–347.

(38) Tang, G.; Peng, L.; Baldwin, P. R.; Mann, D. S.; Jiang, W.; Rees, I.; Ludtke, S. J. EMAN2: An Extensible Image Processing Suite for Electron Microscopy. *J. Struct. Biol.* **2007**, *157*, 38–46.

(39) Pettersen, E. F.; Goddard, T. D.; Huang, C. C.; Couch, G. S.; Greenblatt, D. M.; Meng, E. C.; Ferrin, T. E. UCSF Chimera—A Visualization System for Exploratory Research and Analysis. *J. Comput. Chem.* **2004**, *25*, 1605–1612.

(40) Yang, J.; Yan, R.; Roy, A.; Xu, D.; Poisson, J.; Zhang, Y. The I-TASSER Suite: Protein Structure and Function Prediction. *Nat. Methods* **2015**, *12*, 7–8.

(41) Wood, C. W.; Woolfson, D. N. CCBUILDER 2.0: Powerful and Accessible Coiled-Coil Modeling. *Protein Sci.* **2018**, *27*, 103–111.

(42) Williams, C. J.; Headd, J. J.; Moriarty, N. W.; Prisant, M. G.; Videau, L. L.; Deis, L. N.; Verma, V.; Keedy, D. A.; Hintze, B. J.; Chen, V. B.; Jain, S.; Lewis, S. M.; Arendall, W. B.; Snoeyink, J.; Adams, P. D.; Lovell, S. C.; Richardson, J. S.; Richardson, D. C. MolProbity: More and Better Reference Data for Improved All-Atom Structure Validation. *Protein Sci.* **2018**, *27*, 293–315.

(43) Li, L.; Fierer, J. O.; Rapoport, T. A.; Howarth, M. Structural Analysis and Optimization of the Covalent Association between SpyCatcher and a Peptide Tag. *J. Mol. Biol.* **2014**, *426*, 309–317.

(44) Takayama, Y.; Werbeck, N. D.; Komori, H.; Morita, K.; Ozawa, K.; Higuchi, Y.; Akutsu, H. Strategic Roles of Axial Histidines in Structure Formation and Redox Regulation of Tetraheme Cytochrome C3. *Biochemistry* **2008**, *47*, 9405–9415.

(45) Gibson, D. G.; Young, L.; Chuang, R.-Y.; Venter, J. C.; Hutchison, C. A.; Smith, H. O. Enzymatic Assembly of DNA Molecules up to Several Hundred Kilobases. *Nat. Methods* **2009**, *6*, 343–345.

(46) Arslan, E.; Schulz, H.; Zufferey, R.; Künzler, P.; Thöny-Meyer, L. Overproduction of the *Bradyrhizobium Japonicum* C-Type Cytochrome Subunits of the Cbb3 Oxidase in *Escherichia Coli*. *Biochem. Biophys. Res. Commun.* **1998**, *251*, 744–747.

(47) Zor, T.; Selinger, Z. Linearization of the Bradford Protein Assay Increases Its Sensitivity: Theoretical and Experimental Studies. *Anal. Biochem.* **1996**, *236*, 302–308.

(48) Schneider, C. A.; Rasband, W. S.; Eliceiri, K. W. NIH Image to ImageJ: 25 Years of Image Analysis. *Nat. Methods* **2012**, *9*, 671–675.